

Observed soil arching-induced ground deformation and stress redistribution behind braced excavation

Muchun Liu^{a,b}, Fanyan Meng^{a,c,d}, Zhen Liu^b, and Renpeng Chen^{b,a,c,d}

^aCollege of Civil Engineering, Hunan University, Changsha 410082, China; ^bDepartment of Civil and Environmental Engineering, School of Engineering and Applied Science, University of Virginia, Charlottesville, VA 22903, USA; ^cKey Laboratory of Building Safety and Energy Efficiency of the Ministry of Education, Hunan University, Changsha 410082, China; ^dResearch Center for Advanced Underground Space Technologies of Hunan University, Changsha 410082, China

Corresponding authors: **Fanyan Meng** (email: fymeng@hnu.edu.cn); **Zhen Liu** (email: leoliu@virginia.edu)

Abstract

This paper presents observed arching-induced ground deformation and stress redistribution behind braced excavation using the top-down construction method. The soil properties around the excavation were determined by laboratory and field tests. The ground deformation, soil displacement vector, strain path, principal strain, maximum shear strain, lateral earth pressure, pore water pressure, and effective stress path are presented based on the measured data. The majority of soil behind the wall is under volumetric expansion, indicating consolidation, creep behavior, or a combination of both. Besides, two periods of increases in pore pressure are observed, due to stress transfer from the lower to the upper parts (i.e., soil arching effect). The deep inward movement of the wall and the nearby soil accounts for the distribution of lateral earth pressure acting on the wall. The soil located behind the area of maximum wall deformation and adjacent to the wall, as well as the soil below the excavation base intersected by the shear plane, is in an active stress state. The lateral earth pressure at 5 m from the left excavation wall showed minimal changes, due to the combined effects of soil arching from lateral excavation and shield tunneling.

Key words: excavation, soil arching effect, ground deformation, lateral earth pressure, effective stress path

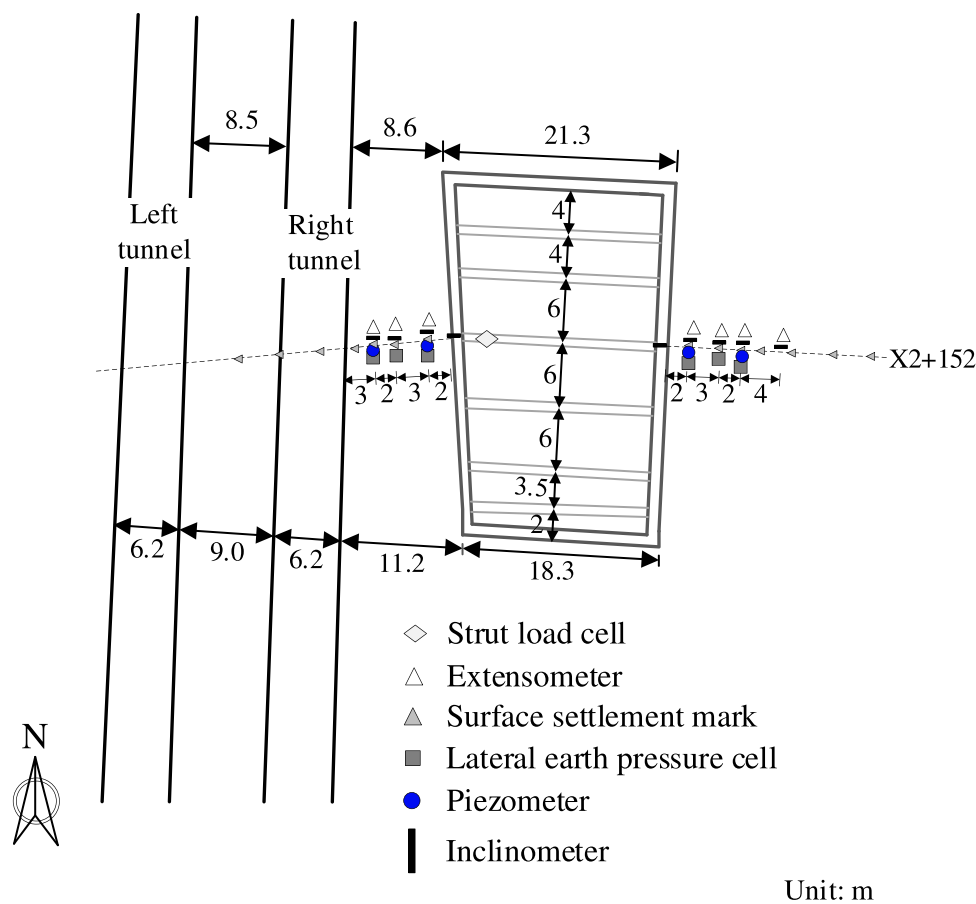
Introduction

In recent decades, the rapid development of underground space in cities has led to numerous deep excavation constructions (Liu et al. 2005, 2011; Yang et al. 2011; Tan and Wei 2012; Ou 2014; Hong et al. 2015; Meng et al. 2021). The main challenge in deep excavation is to ensure the safe construction of the excavation and to mitigate potential impacts on nearby existing structures (Bolton 1993; Ng et al. 2003; Tan and Li 2011; Bolton et al. 2014; Faustin et al. 2017; Meng et al. 2022a; Liu et al. 2023). For example, excavation in Shenzhen resulted in the cumulative horizontal and vertical displacements of the shield tunnel of Metro Line 1 located 38 m away to reach 34.8 and 76.8 mm, respectively, which caused severe cracking and water leakage in the tunnel lining (Zhu et al. 2019). Therefore, one essential issue for the design of braced excavations is the determination of the ground deformation and stress redistribution behind the wall. This is closely related to the soil arching effect. However, there are limits in considering the arching-induced ground deformation and stress transfer behind the excavation, resulting in inaccurate prediction for deformation and stress in the soil mass. Therefore, it is necessary to investigate the soil arching effect behind the excavation to ensure the ser-

viceability and safety of both the excavation and existing structures.

Numerical simulations (Hashash and Whittle 2002; Karlsrud and Andresen 2005; Meng et al. 2022b; Liu et al. 2023) and theoretical analyses (Mindlin 1936; Sagaseta 1987; Lei et al. 2001; Osman and Bolton 2005; Kung et al. 2007; Cheng et al. 2020) have been employed to understand the complex behavior of soil during excavation. However, there are various factors influencing the soil response, and making it challenging to obtain accurate predictions solely from these methods. Therefore, field measurements, which provide direct observations of the actual soil behavior, are necessary for obtaining reliable and precise data for a better understanding of the arching-induced deformation and stress redistribution behind the excavation. The soil arching effect is one of the most common phenomena encountered in geotechnical engineering (Terzaghi 1943), including tunneling, piled embankments, excavations, and so on. To date, however, the field measurements that reveal the soil arching effect behind the excavation are very limited compared with that caused by shield tunneling and piled embankments, with only a few studies conducted by Lambe and Whitman (1969), Ng et al. (2012), Li et al. (2021), Liu (2022), Yang

Fig. 1. Plan view of the construction site with instrumentations.



et al. (2023), and Chen et al. (2023). Besides, attention from previous studies on the arching effect is usually put on the ground deformation but seldom took into account both ground movement and stress transfer, which are the two characteristics of the arching effect. There is only a limited amount of measured data available regarding the soil strain path and effective stress path induced by lateral excavation. Very limited field data are also found for the principal strain and maximum shear strain behind the braced excavation. The mechanism of arching-induced ground deformation and stress redistribution during excavation remains to be studied. These limit the assessment of the responses of the nearby ground and existing structures and the development of corresponding countermeasures.

In an attempt to address the aforementioned issues regarding the excavations, a braced excavation in Wuhan clayey ground was heavily instrumented. The soil properties in this site were determined by laboratory and field tests. The monitoring program includes measurement of horizontal and vertical ground movement, ground surface settlements, diaphragm wall deformation, earth pressure, pore water pressure, and strut load. The ground deformation and stress redistribution associated with the arching effect were studied through further analysis of the measured data, including soil displacement vector, strain path, principal strain, maximum shear strain, lateral earth pressure, pore water pressure, and effective stress path.

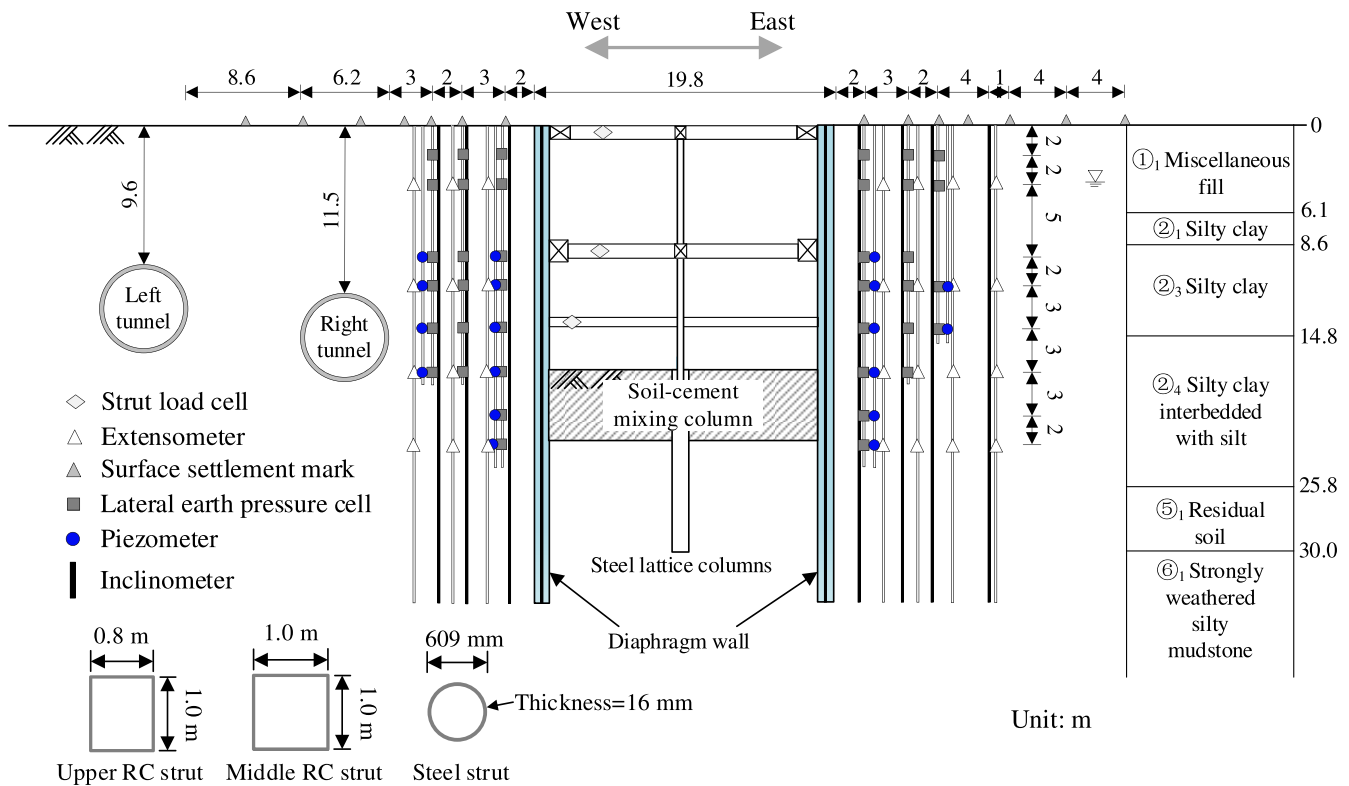
Site characterization

Retaining system and nearby tunnel

The excavation studied in this paper is associated with the construction of a city expressway named the South Extension of Peace Avenue in Wuhan, Hubei Province, China. The excavation exhibited an approximately trapezoidal shape, as depicted in Fig. 1. The width of the excavation ranged from 18.3 to 21.3 m, and the length was 31.5 m. Focus is paid to the center cross-section X2 + 152 to observe the two-dimensional ground responses.

As shown in Fig. 2, the excavation was supported by a 33.5 m deep and 1 m wide diaphragm wall and three levels of temporary internal bracing. The top and middle levels of internal bracing each consisted of a pair of reinforced concrete (RC) struts measuring a cross-sectional height of 1 m and a width of 0.8 or 1 m. They were supported vertically by steel lattice columns at their midpoints. The horizontal axial spacings of the RC struts were 3.5, 6, and 4 m, respectively. The bottom level of internal bracing was steel casing pipes measuring 0.609 m in outer diameter and 0.016 m in thickness. To ensure a stiff retaining system, purlins were welded between the RC struts and rows of reinforcement protruding from the diaphragm wall, enabling the RC struts to be in rigid connection with the wall. The loads from the retained soil were transferred to the struts via the purlins. In addition, the excavation bottom was reinforced by soil-

Fig. 2. Transverse view with instrumentations on Section X2 + 152. RC, reinforced concrete.



cement mixing columns with depths ranging from 4.8 to 6.0 m.

The shield tunnels lay parallel and west to the excavation, with twin tunnels featuring staggered joints. The outer boundary was 8.5–9.0 m from the excavation, and the distance between the right-line tunnel and the excavation ranged from 8.6 to 11.2 m, with its cover depth at 11.1–11.8 m. The tunnel and excavation base were at a similar depth. The lining of the tunnel was 1.5 wide, with internal and external diameters of 5.5 and 6.2 m, respectively, and a thickness of 0.35 m.

Ground conditions

Wuhan is situated at the confluence of the Han River and the Yangtze River in the eastern part of the Jiangnan Plain, which lies in the middle reaches of the Yangtze River. The construction site fell within the first- and third-order terraces of the Yangtze River alluvial plain. Before excavation, the ground condition at the construction site was fully investigated by a series of field tests such as standard penetration tests and cone penetration tests, and laboratory tests, including standard oedometer tests and triaxial tests.

The ground level was taken as the reference datum. As shown in Fig. 3, the strata concerned in this excavation were composed of six layers with a total depth of up to 40 m. Generally, the subsurface conditions consisted of a layer of ① miscellaneous fill with a thickness of 6.0 m, followed by a thick layer of compressible ② clayey soils ranging from depths 6.0

to 27.9 m. The underlying soil comprised ⑤ residual soil at an average depth ranging from 27.9 to 30.0 m and ⑥₁ strongly weathered silty mudstone at a depth of 29.3–40.0 m. The ② clayey soils influenced the excavation significantly and the shield tunnel located within ②₃ silty clay and ②₄ silty clay interbedded with silt. The long-term groundwater table level was observed approximately hydrostatic at 4.1 m below the ground surface.

The average geotechnical parameters of the investigated layers are summarized in Table. 1. Using average soil properties is reliable in this study due to the rigorous collection and analysis methods employed. The soil data, aligned with Phoon and Kulhawy’s (1999) standards, were collected from similar geological origins and within confined spatial extents using robust equipment and procedural controls, thereby minimizing spatial variability. The limited scale of this excavation and minimal longitudinal variations in soil properties further validate the use of average values. These factors collectively ensure that the average soil properties accurately reflect the inherent characteristics of the excavation, making them suitable for precise geotechnical analysis and design.

The boundary water content of each specimen was measured using a photoelectric liquid–plastic limit combined measuring device. Taking ②₁ silty clay as an example, the typical result from standard oedometer tests and triaxial tests are shown in Fig. 4. The parameters (E_s , E , m) were obtained by standard oedometer test on the undisturbed soil sample. Pre-consolidation pressure and over-consolidation ratio of the soil were obtained by using Becker’s method

Fig. 3. Longitudinal view of the excavation and soil profile.

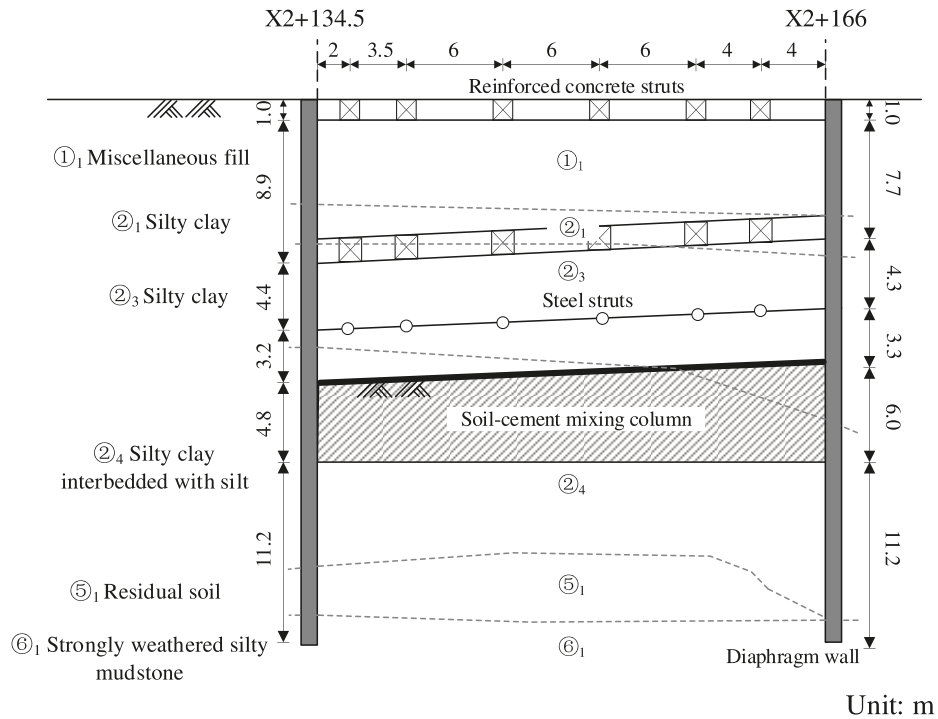


Table 1. Average geotechnical parameters.

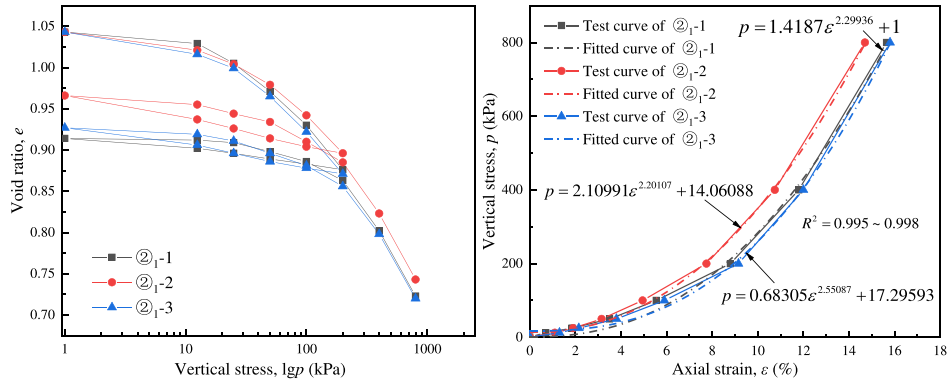
Number	① ₁	② ₁	② ₃	② ₄	⑤ ₁	⑥ ₁
w (%)	27.8	34.3	24.3	24.1	23.5	26.4
γ (kN/m ³)	17.9	17.9	19.7	19.7	19.4	20.5
e_0	0.917	1.043	0.711	0.714	0.679	/
G_s	/	2.72	2.72	2.71	2.7	/
I_p (%)	/	15.9	15.1	14.7	/	/
I_L	13.9	0.689	0.417	0.446	/	/
E_s (kPa)	5000	4097	8473.7	9874.7	12500	38300
$E_{\text{oad}}^{\text{ref}}$ (kPa)	5000	3440.4	6585.7	7777.3	12500	38300
E_{50}^{ref} (kPa)	5000	3931.5	7043.3	8226.0	12500	38300
$E_{\text{ur}}^{\text{ref}}$ (kPa)	15000	42859.2	50315.4	33375.7	37500	114900
ν	0.32	0.37	0.28	0.39	0.3	0.25
m	0.5	0.60	0.72	0.65	0.65	0.5
c' (kPa)	10	13.7	4.7	12.7	13	14
ϕ' (°)	25	25.8	31.8	28.4	33	36
ψ (°)	0	0	0.55	0.17	0	0
R_f	0.9	0.81	0.87	0.70	0.9	0.9
q_u (kPa)	/	63.1	70.9	98.3	/	/
SPT-N	/	3.5	3.0	4.0	18	34
OCR	/	1.1	1.07	1.06	1.06	/

Note: w = water content; γ = unit weight; e_0 = void ratio; G_s = specific gravity; I_p = plasticity index; I_L = liquidity index; E_s = compression modulus; $E_{\text{oad}}^{\text{ref}}$ = reference stiffness from one-dimensional compression tests; E_{50}^{ref} = reference secant stiffness of trial axial compression stress paths; $E_{\text{ur}}^{\text{ref}}$ = reference stiffness for unloading/reloading stiffness; ν = Poisson's ratio; m = power that controls the stress dependency of stiffness; c' = effective cohesion; ϕ' = effective inner friction angle; ψ = dilatancy angle; R_f = failure ratio; q_u = unconfined compression strength; SPT-N = standard penetration test counts; OCR = over-consolidation ratio.

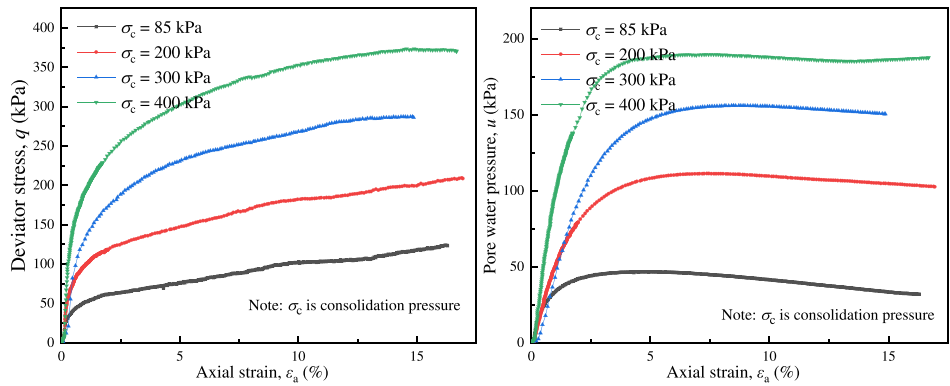
(Becker et al. 1987) toward the oedometer test results. This test was performed using a step-by-step loading-unloading-reload method, with a maximum applied load of 800 kPa. The unloading intervals ranged from 200 to 1 kPa with a reduc-

tion of half load for each increment. Once the deformation of the soil sample stabilized under a particular stress level, unloading to the subsequent stress level was performed. The compression modulus E_s roughly increased with the depth,

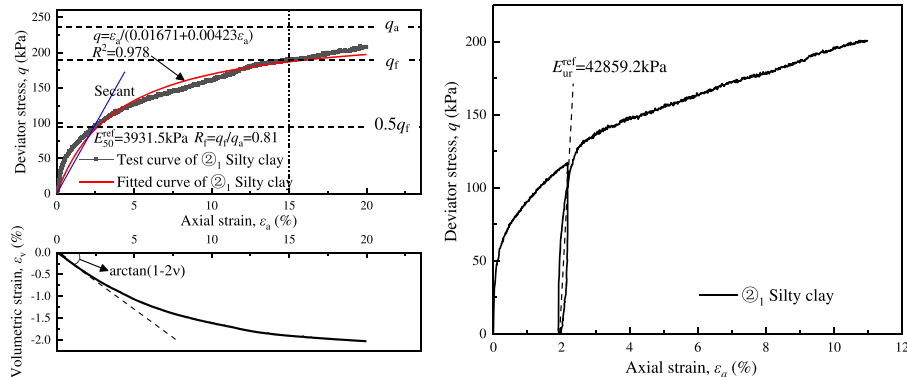
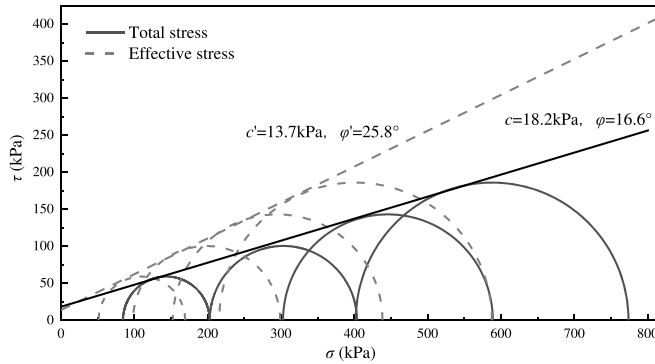
Fig. 4. Laboratory test results of ②1 silty clay: (a) oedometer test; (b) consolidated undrained triaxial test; and (c) consolidated drained triaxial test.



(a)



(b)



(c)

Can. Geotech. J. Downloaded from cdnsiencepub.com by UNIVERSITY OF VIRGINIA on 05/06/25 For personal use only.

Table 2. Construction stages.

Stage		Date (mm/dd/yyyy)	Days spent	Construction activity
Pre-excavation	0(a)	04/29/2021–05/10/2021	12	Construct grouted struts (–16.9 to –22.3 m)
	0(b)	05/15/2021–05/20/2021	6	Excavate shallow soil (0 to –1.0 m)
	0(c)	05/21/2021–05/28/2021	8	Install first-level RC struts (0 to –1.0 m)
Main-excavation	1(a)	05/29/2021–06/13/2021	16	Excavate first layer (–1.0 to –9.3 m)
	1(b)	06/14/2021–06/22/2021	9	Install second-level RC struts (–8.3 to –9.3 m)
	2(a)	06/23/2021–07/14/2021	23	Excavate second layer (–9.3 to –13.7 m)
	3(a)	07/15/2021–07/24/2021	10	Excavate third layer (–13.7 to –16.9 m)
	3(b)	07/25/2021–07/27/2021	3	Install third-level steel struts (–13.3 to –13.9 m)
	3(c)	07/28/2021–08/03/2021	7	Cast base slab (–15.6 to –16.9 m)
After-excavation	4(a)	08/04/2021–08/06/2021	3	Remove third-level steel struts (–13.3 m to –13.9 m)
	4(b)	08/07/2021–08/23/2021	17	Construct middle slab (–10.3 m to –11.0 m)
	4(c)	08/24/2021–08/27/2021	4	Remove second-level RC struts (–8.3 to –9.3 m)
	4(d)	08/28/2021–09/11/2021	15	Construct top slab (–4.5 to –5.7 m)

with ②₃ silty clay and ②₄ silty clay interbedded with silt in the parameter. Multiple triaxial tests were conducted on the clays to obtain corresponding strength and stiffness parameters, where each soil specimen was consolidated isotropically before shearing. More details can be found in the companion paper (Chen et al. 2023).

Around the construction site, the thickness of each soil stratum was relatively uniform. This made it possible to compare excavation-induced deformation and stress at different locations of the site.

Construction sequence

A top-down excavation method was employed for the excavation. Before excavation, the diaphragm wall was constructed and the ground below the excavation base was reinforced by soil–cement mixing columns to form “grouted struts”. They span the entire excavation with a diameter measuring 0.85 m with an axial spacing of 0.6 m. After excavating the shallow soil, the first-level RC struts were constructed along the top of the whole diaphragm wall through the intermediary of purlins, which enhanced the total retaining system stiffness. Due to the small excavation area, zoned excavation was not adopted. The main excavation involved alternating cycles of excavation and installing struts. The first-level and second-level struts were made of RC, while prestressed steel struts were used on the third level. Soil excavation proceeded only after RC struts reached 70% of their maximum strength, ensuring safety and structural integrity. This practice, acknowledging RC structures’ capability to withstand loads exceeding 75% of their short-time capacity without failure, employs the 70% threshold as a safety margin (Ma 2021). This balanced construction progress with stability under different load conditions. To meet the projected construction schedule, the installation of third-level struts was postponed until the final excavation depth was reached. Following the completion of the base slab construction, the third-level steel struts were removed and a middle slab was cast above their place. The installation procedure for the top slab was identical to the middle slab. The detailed construction stages can be found in Table 2.

Instrumentation

To improve understanding of the arching-induced ground deformation and stress redistribution behind the braced excavation, various instruments were heavily installed at the construction site, especially the excavation center (Section X2 + 152). In this paper, the data obtained from lateral earth pressure (EP) cells, piezometers, strut load cells, inclinometers, extensometers, and ground surface settlement marks were presented (refer to Figs. 1 and 2). The resolution and accuracy of instruments are shown in Table 3.

To measure the lateral earth pressures at varying distances behind the wall, several vibrating wire EPs were installed on both sides of Section X2 + 152. Each EP was accompanied by a piezometer (P) situated at the same depth as the Ps to measure corresponding pore pressures so that the effective earth pressure could be captured. The initial readings of the EPs and Ps were recorded and calibrated against the corresponding lateral earth pressure at the same depth and hydrostatic water pressure at each depth, respectively. The EP was firmly fixed to the grooves of the tube, which was then gradually lowered into the borehole and secured with screws. The EP was oriented toward the excavation to measure lateral earth pressure. Once the tube was fully inserted into the borehole, the gaps between the tube and the soil were quickly filled with bentonite balls, clay, and sand. The inside of the tube was also filled with bentonite balls, which absorbed water and expanded to squeeze the EP outward, making it in firm contact with the outside soil. The installation of the piezometer was similar to the EPs. The piezometer was fully saturated by immersing it in clean water for more than 24 h. Subsequently, it was lowered by using a rope to a specific depth in a borehole that was partially filled with slurry. Once the desired depth was reached, the rope was fixed and the gap between the borehole and the piezometer was filled. The top of the slurry in the borehole was identical to the groundwater table.

The installation process for inclinometers and extensometers involved several steps. Inclinometers were installed both in the diaphragm wall and surrounding ground, with careful consideration of depth, alignment, and error correction. In

Table 3. Resolution and accuracy of instruments.

Instrument	Piezometer (P)	Lateral earth pressure cell (EP)	Load cell	Inclinometer probe	Extensometer	Leveling
Resolution	0.3 kPa	0.3 kPa	1.6 kN	0.1 mm/500 mm gauge length	0.015 mm	±0.5 mm/km
Accuracy	2.0 kPa	2.0 kPa	3.0 kN	0.1 mm/500 mm gauge length	0.25 mm	±0.5 mm/km

the installation process, it was specified that instrumentation boreholes should extend about 10 m deeper than the final excavation depth. This was aimed at reaching into the ground where movement is minimal, ensuring more stable and reliable readings (Schwamb et al. 2016). The process involved taking multiple initial readings, which were later averaged to enhance accuracy and repeatability.

The inclinometers were fixed to reinforcement cages before casting concrete to measure wall deflection. The horizontal ground movements were also measured by the inclinometers embedded into the borehole behind the wall. The inclinometers had a pair of grooves oriented in the expected measured direction of movement. These inclinometers were installed behind the wall at a distance of 2, 5, 7, and 11 m. However, due to the presence of the tunnel, an inclinometer was not installed at a distance of 11 m on the left side. The inclination was measured using probes with a resolution of 0.1 mm over a 500 mm gauge length.

The magnetic extensometers with a resolution of 0.015 mm for measuring vertical ground movements were attached to the tubes, which were lowered section by section into the borehole. The bottom tube was positioned on the bedrock to ensure absolute displacement measurements. The magnetic claws of each extensometer were securely anchored into the ground so that the claws could simultaneously move vertically with the ground and the extensometer could measure the vertical ground displacement. Extensometers were positioned at the excavation center, at intervals of 2, 5, 7, and 11 m behind the diaphragm wall, and depths of 4, 11, 17, and 22 m below the ground surface.

Markers for measuring ground surface settlement were buried 0.5 m below the ground surface and perpendicular to the excavation. The markers were positioned at varying distances from the diaphragm wall, specifically at intervals of 2, 5, 7, 9, 12, 16, and 20 m. The markers were measured by level with a resolution of 0.5 mm/km, concerning a benchmark socket located approximately 85 m (equivalent to five times excavation depth) behind the wall. The measurements from the inclinometer, surface settlement marks, and extensometer captured the direction and magnitude of the ground movements.

The loads on each strut were determined by measuring the strains using vibrating wire strain gauges. Subsequent changes in strain from the initial values were used to calculate the loads applied to the struts. To reduce the impact of temperature, the strut loads were measured daily in the evenings.

All monitoring instruments were initiated to start measuring in the stage of pre-excavation. Emphasis is put on the measured results during the main excavation (from 29 May 2021 to 24 July 2021). The measured data were minimally

time-affected after reaching the final excavation depth due to the fast casting of the slabs following excavation.

Interpretation of measured results

This paper distinctively focuses on the two-dimensional effects of braced excavation in the clayey ground, incorporating analyses of soil displacement vectors, strain path, shear strain, effective stress, and pore water pressure. In contrast, the companion paper (Chen et al. 2023) concentrates on three-dimensional ground responses, primarily investigating aspects like partitioning the soil arching and total lateral earth pressure, without delving into the parameters this paper explores.

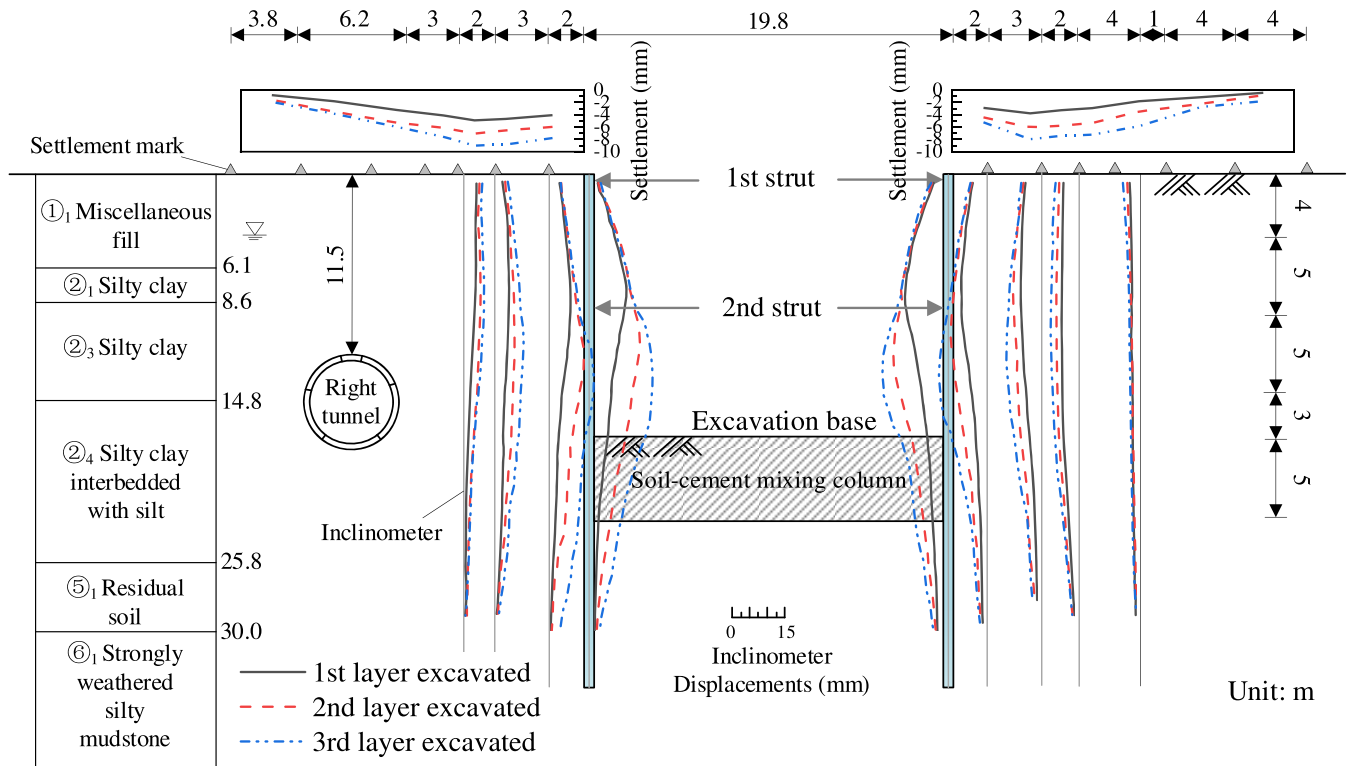
General ground deformation

The general ground response throughout excavation in this part was described by examining the diaphragm wall, and horizontal and vertical ground displacements. In this study, settlement is considered negative and heave is regarded as positive, aligning with the conventions used in Tan and Wang (2013b), Li et al. (2021), and Yang et al. (2023). As depicted in Fig. 5, both the diaphragm wall and the ground near the wall exhibited inward concave (deep-seated) deformations. This matched trends seen in other deep excavation databases, particularly showing the typical deep-seated deformation detailed by Hsieh and Ou (1998).

This phenomenon can be attributed to the installation of the initial RC strut before excavation, which restricted deformation at the wall's top. Initially, maximum wall deflection was observed around the second strut. However, as excavation continued, this point of maximum deflection shifted deeper, paralleling the excavation depth. The maximum wall deflection recorded was 16.7 mm, representing roughly 0.1% of the total excavation depth. The normalized wall deformation observed varied between 0.03% and 0.1%, aligned with the minimal range of normalized wall deformation in Shanghai soft clay reported by Tan and Wang (2013a). These normalized values fell within the range of 0.2%–0.5% excavation depth for those summarized by Ou et al. (1993). These findings were less than Clough and O'Rourke's (1990) maximum deformation of 0.2% excavation depth in stiffer soils and Peck's (1969) data of 1% excavation depth, which primarily involved pile-supported lateral systems.

Furthermore, the maximum horizontal displacement increased with distance from the wall and gradually shifted toward the ground surface, forming a cantilever-shaped profile of horizontal ground displacement. This phenomenon is consistent with the case histories observed by Li et al. (2021) and Yang et al. (2023). The tunneling-induced disturbance caused

Fig. 5. Transverse ground horizontal displacements and surface settlements on Section X2 + 152.



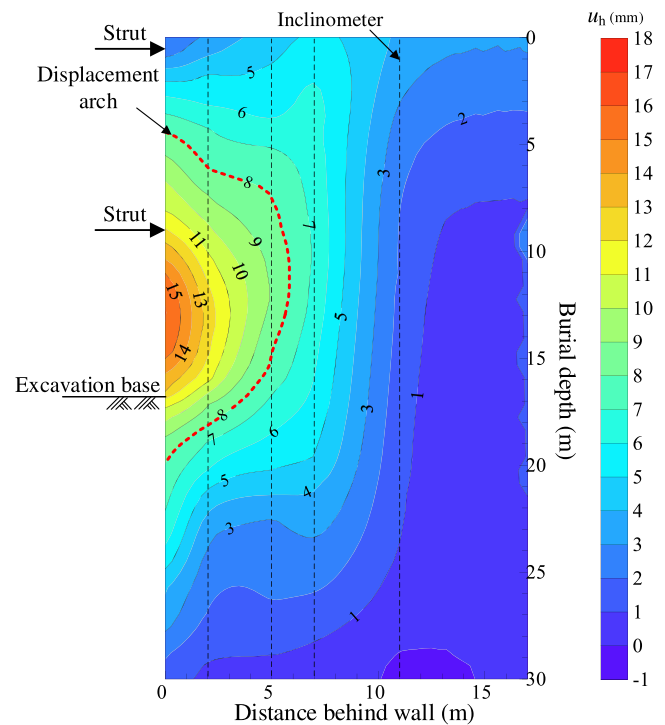
a reduction in the strength and stiffness of the surrounding soil (Meng et al. 2018), resulting in slightly greater horizontal displacement on the left side compared to the right side.

Deep inward movement presented by the wall, accounted for the maximum surface settlement occurring at some distance from the wall. The maximum ground surface settlement was located about 5 m behind the wall, recorded at -9 mm and accounting for 0.053% of the excavation depth. This concave surface settlement pattern corresponded to the deep-seated deformation of the wall, which was a typical settlement profile observed by Hsieh and Ou (1998). The settlement trough extended to approximately 1.5 times the excavation depth behind the wall. The ratio of the maximum surface settlement to the maximum wall deformation was 0.54, which was similar to the field measurement of 0.56–0.78 by Ou et al. (1998), and was also generally within the range of the findings by Clough and O’Rourke (1990).

Figure 6 depicts the contours of horizontal ground displacement after the third layer excavated, which were derived through a combination of measured inclinometer data and Kriging interpolation. It was assumed that the soil located beyond three times the excavation depth from the wall was minimally impacted by excavation, and therefore the ground displacement at these distant locations was considered zero (Ou et al. 2000).

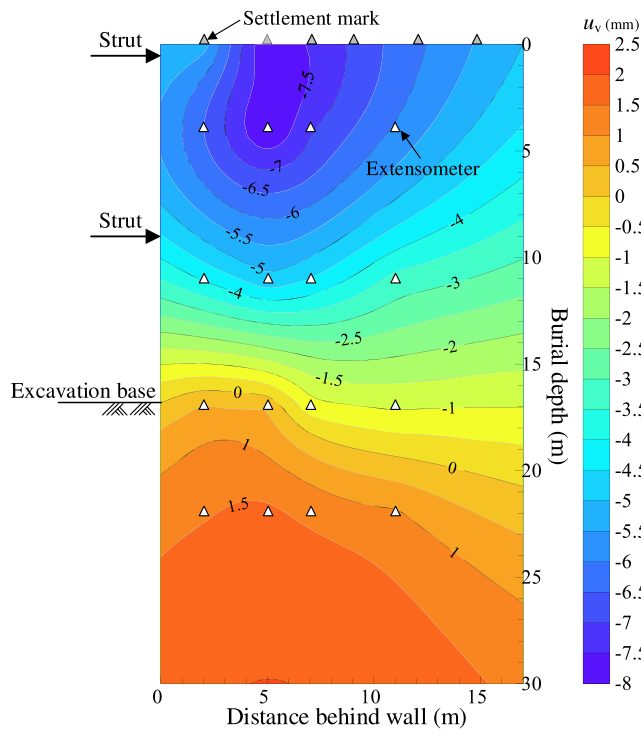
Kriging is a widely used geostatistical method for generating interpolated contours from scattered data. It is recognized as an effective method in environmental and spatial studies for modeling spatial correlations with associated uncertainties (Trochu 1993). A standard deviation grid was incorporated to quantify uncertainty, and Point Kriging, tailored to the specific characteristics of the data, was employed

Fig. 6. Contour of horizontal ground displacement on Section X2 + 152 after the third layer excavated.



for a more nuanced spatial analysis. Additionally, monitoring points were densely placed at the excavation center to minimize interpolation uncertainties, thus enhancing the accu-

Fig. 7. Contour of vertical ground displacement on Section X2 + 152 after the third layer excavated.



racy of the findings. This approach, balancing raw data representation with the inherent uncertainties of interpolation, aligns with methodologies used in recent field studies (Li et al. 2021; Yang et al. 2023), validating the correctness of the interpolated data in corresponding figures.

As shown in Fig. 6, the soil near the top of the wall and the excavation base showed minimal horizontal displacement. In contrast, the soil behind the maximum wall deformation experienced the most significant horizontal movement. The relative movements between the two parts resulted in the formation of a horizontal displacement arch visibly marked in Fig. 6 with red dash lines. This phenomenon was similar to that observed in Terzaghi's trapdoor test and shield tunneling, where the soil arching effect occurred. It was due to that the soil displacement behind the maximum wall deformation was greater than that at the neighboring parts, resulting in the resistance of shear strength and the stress transfer from the soil behind maximum deformation to the adjacent relative stationary parts. In other words, the maximum wall deformation was akin to that of the downward trapdoor or shield tunnel machine, while the distinction was that the wall was continuous, whereas the other two were separate.

Figure 7 displays the contours of vertical ground displacement after the third layer excavated, which were obtained from extensometer measurements and Kriging interpolation. An obvious settlement concentration zone in the shallow soil was observed, with the maximum settlement occurring approximately 5 m away from the wall. This was consistent with the location of the maximum ground surface settlement. The ground settlement within the shallow depth was

greatest and decreased gradually with depth. In Terzaghi's trapdoor test, the trapdoor's downward movement aligned with gravity direction, predominantly causing vertical soil displacement. In contrast, the equivalent "trapdoor" in the context of excavation moved horizontally, intersecting with gravity and thereby inducing both horizontal and vertical soil displacements. The dominant horizontal displacement results in a less apparent vertical displacement arch, while the horizontal displacement arch is more pronounced.

Displacement vector

To comprehensively analyze the trends of soil movement, Figs. 8 and 9 present the vectors illustrating the soil movements behind the wall during stages 1(a)–3(a). These figures were obtained based on inclinometer measurements for horizontal displacements and extensometer measurements for vertical displacements.

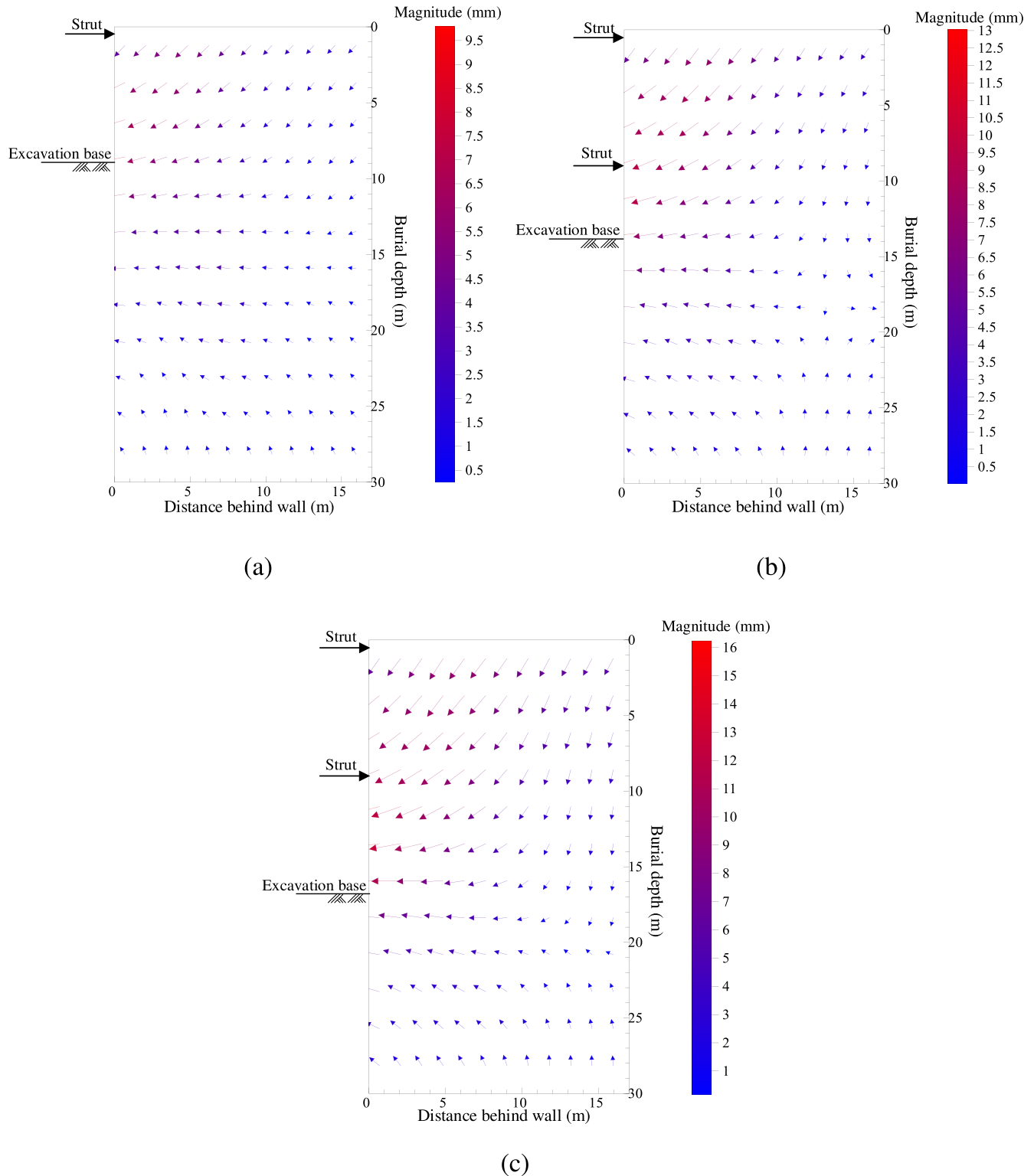
The displacements, particularly within the clays above the excavation base, were oriented at approximately 45° and indicated progressive movements toward the wall, while the soil below the excavation base showed an upward movement toward the wall. The vertical displacements of the soil at the depth of the excavation base were insignificant, with dominant horizontal displacements toward the wall. In fact, there was a tendency for the displacement vectors to be oriented toward the excavation base. The movements increased with the excavation depth. These incremental movements were indicative of a block-type movement that was associated with the development of a shearing plane. A similar response was observed in the case history reported by Finno et al. (1989b). The areas with larger displacement vectors were concentrated above the excavation base, within approximately 0.6 times the excavation depth from the wall. The deformations were larger as closer to the wall, and the maximum displacement reached approximately 16 mm, which was about 0.95 times the excavation depth.

As shown in Fig. 9, the horizontal displacements of the soil near the wall were observed considerably larger than the vertical displacements, while that far from the wall usually exhibited less than the vertical displacements. In other words, the ratio of vertical displacement to horizontal displacement increased with the distance from the wall. Furthermore, the maximum vertical soil movement did not occur at the ground surface, but rather about 4 m below the surface. This suggested that the soil movements were not uniform throughout the depth behind the wall, with differences observed at different depths. Besides, the incremental vectors of soil movement were mainly concentrated during the first and second layers of excavation, which was due to the deeper excavation level in these two stages.

Strain path

The soil strains were computed from the inclinometer, extensometer, and ground surface settlement mark measurements using the method proposed by Finno and Nerby (1989a). The horizontal strain ε_h components were computed from inclinometer measurements by dividing the differential horizontal displacement by the initial horizontal distance.

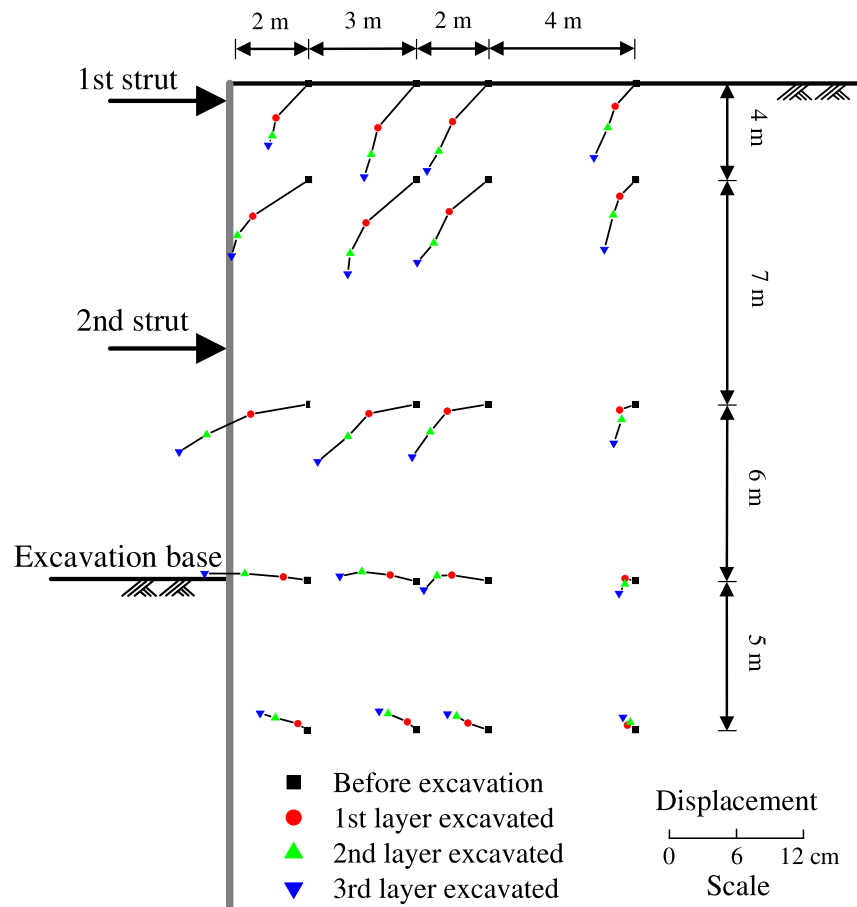
Fig. 8. Ground movement vectors on Section X2 + 152 during excavation: (a) first layer excavated; (b) second layer excavated; and (c) third layer excavated.



The vertical strain ε_v components were computed from extensometers and settlement marks by dividing the differential vertical movements by the initial vertical distance. The shear strain ε_{hv} components were half the sum of the angular distortions ($\Delta u/\Delta y + \Delta v/\Delta x$). This method was com-

monly used in computing ground strain (Finno and Nerby 1989a; Ou et al. 2000; Li et al. 2021; Chen et al. 2023; Yang et al. 2023). The soil strain paths at stages 1(a), 2(a), and 3(a) were derived from strain magnitudes at the midpoint between the two measured points. Positive values indicated

Fig. 9. Incremental vectors of the soil movements during excavation on Section X2 + 152.



tensile strain for horizontal and vertical strain, while negative values represented compressive strain, and the shear strain was presented by the absolute values. The installation of densely distributed monitoring points could ensure the accuracy and reliability of the fixed midpoint for strain calculation.

As shown in Fig. 10a, the ε_h and ε_v increased with the excavation depth. The majority of the soil located behind the wall experienced horizontal extension and vertical compression, except for the soil near the crest of the wall and at shallow depths, which was subjected to horizontal compression and vertical extension. This phenomenon was consistent with the measured lateral earth pressure, which at shallow depth appeared to exceed the initial values and that at deep levels was lower than the initial values (described below).

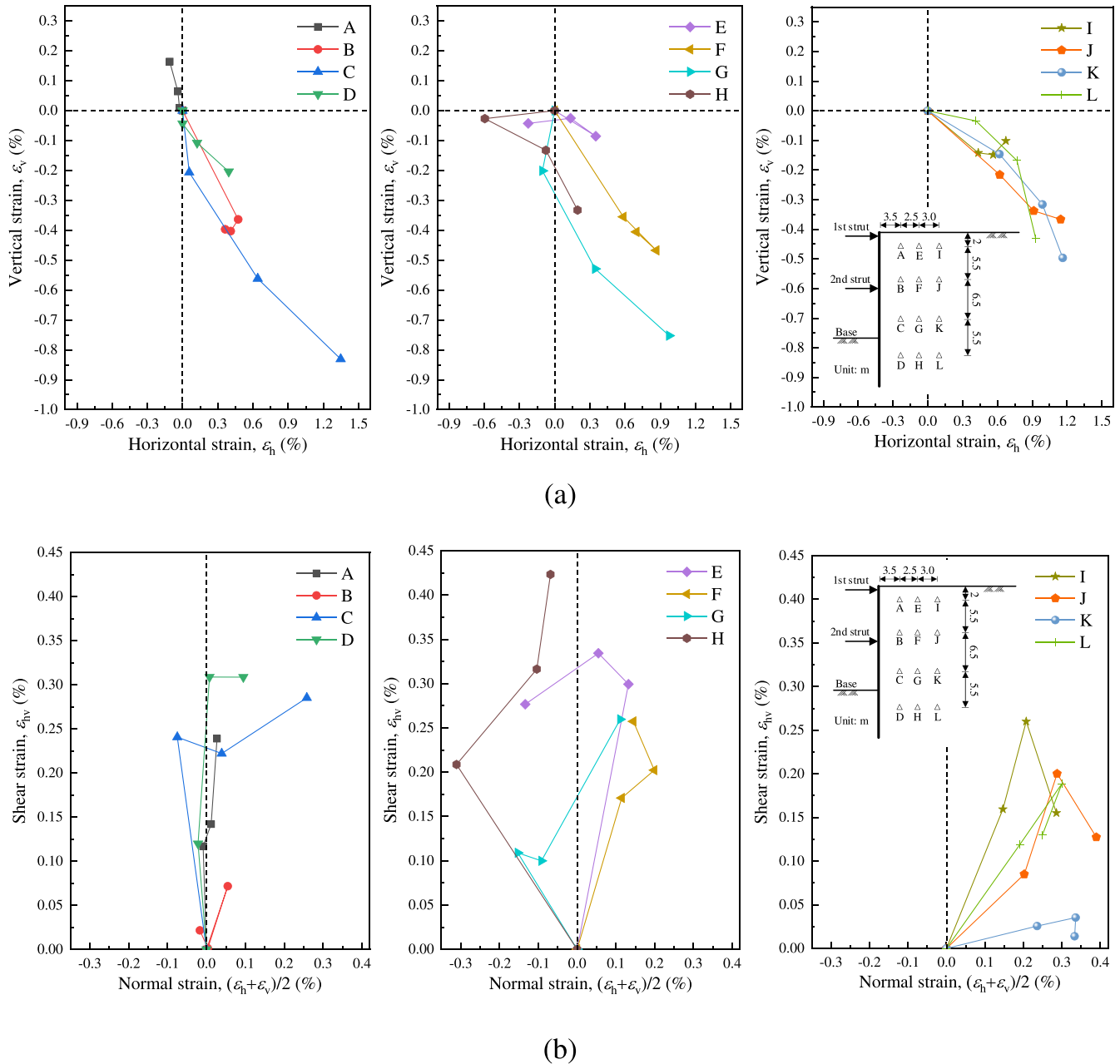
The maximum horizontal and vertical strains were concentrated behind the maximum wall deformation, specifically at points C, G, and K. This demonstrated that the soil behind the maximum wall deformation was under a larger horizontal extension and vertical compression. Furthermore, as the distance from the wall increased, the corresponding strain decreased. The maximum horizontal tensile and compressive were 1.35% and -0.11% , respectively, and the corresponding vertical strains were 0.16% and -0.83% , respectively. The ratio between maximum horizontal and vertical strains was 1.63,

indicating that the soil strain in the lateral excavation was mainly under horizontal extension.

As shown in Fig. 10b, the horizontal axis represents soil volumetric change, while the vertical axis represents shear strain. Except for points E and H, the volumetric strains in the measured soil points during the excavation process were slightly greater than zero. This indicated that the majority of the soil behind the wall experienced volumetric expansion (positive values on the horizontal axis), except for points E and H, where volumetric compression was observed. Although the volumetric expansion was consistent with excavation unloading, it was noteworthy that the excavation actually took place under undrained loading conditions, and the volumetric change should ideally be zero. However, most of the soil exhibited nonzero volumetric changes. This suggested that there could have been consolidation or creep effects, or both, in the saturated clay due to water movement during excavation.

The strain paths of points E and H revealed lateral compression existed within the soil mass, induced by the incremental movement of the soil toward the braced portions of the wall. In addition, the soil at point H located below the excavation base was sheared significantly, which possessed the maximum shear strain of 0.42%. This demonstrated that the shear plane was developed around the wall below the excavation base and passed through point H.

Fig. 10. Strain paths: (a) relationship between horizontal strain and vertical strain and (b) relationship between normal strain and shear strain.



Principal strain

Figure 11 shows the principal strain increments at stage 3(a), derived based on horizontal, vertical, and shear strain using the theory of Mohr’s circle; the calculation equation is shown below:

$$(1) \quad \epsilon_1, \epsilon_2 = \frac{\epsilon_h + \epsilon_v}{2} \pm \sqrt{\left(\frac{\epsilon_h - \epsilon_v}{2}\right)^2 + \left(\frac{\gamma_{hv}}{2}\right)^2}$$

$$(2) \quad \tan 2\theta = \frac{\gamma_{hv}}{\epsilon_h - \epsilon_v}$$

where ϵ_1 and ϵ_2 are major and minor principal strains, respectively; ϵ_h and ϵ_v are horizontal and vertical

strains, respectively; γ_{hv} is the shear strain; and θ is the angle between principal direction and horizontal direction.

The majority of the soil behind the wall was in a state of lateral or near-lateral extension. This phenomenon was consistent with the observed strain increments shown in Fig 10. Notably, the magnitudes of the principal strain increments were found to be larger in the soil near the excavation base compared to other areas. This suggested that the soil behind the excavation base experienced relatively higher levels of strain, due to the maximum lateral wall deformation occurring near the excavation base. Besides, the directions of the principal strain increments of the soil below the excavation base were also inclined much more than in any other part of

Can. Geotech. J. Downloaded from cdnscepub.com by UNIVERSITY OF VIRGINIA on 05/06/25
For personal use only.

Fig. 11. Principal strain increments on Section X2 + 152.

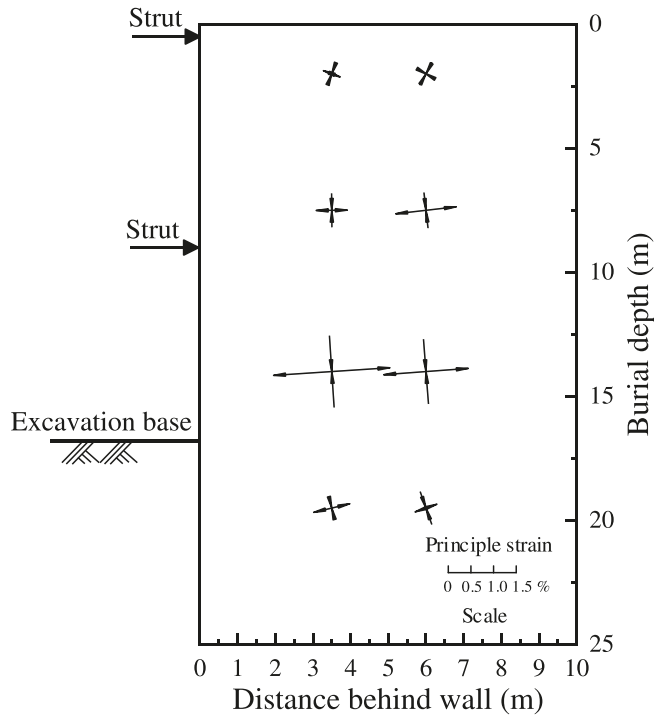
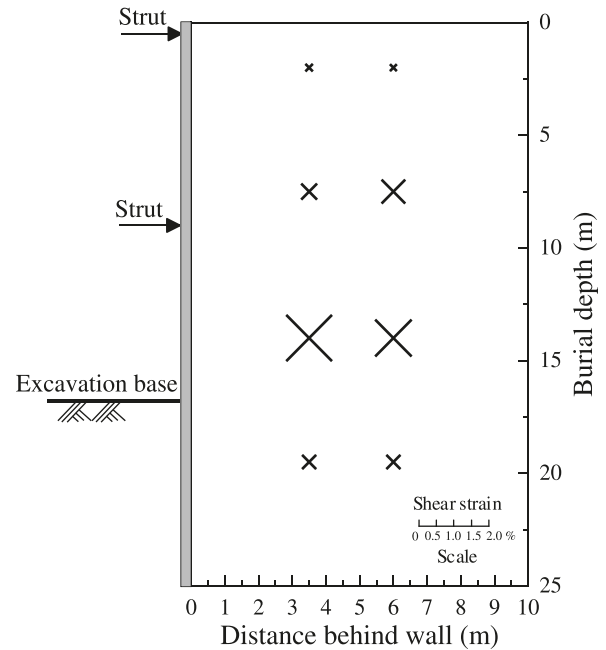


Fig. 12. Maximum shear strain on Section X2 + 152.



the soil, which was associated with the development of the shear plane.

Maximum shear strain

Figure 12 shows the maximum shear strain at stage 3(a), calculated from horizontal, vertical, and shear strain using the following equation:

$$(3) \quad \frac{\gamma_{\max}}{2} = \sqrt{\left(\frac{\epsilon_h - \epsilon_v}{2}\right)^2 + \left(\frac{\gamma_{hv}}{2}\right)^2}$$

where γ_{\max} is the maximum shear strain; ϵ_h and ϵ_v are horizontal and vertical strains, respectively; and γ_{hv} is the shear strain.

The maximum shear strain within the soil mass was oriented at 45° and developed behind the maximum wall deformation, which was consistent with the strain path in Fig. 10. In fact, the increment of maximum shear strains demonstrated the unmistakable formation of a zone of concentrated shear strains in a distinct zone behind the maximum wall deformation. The maximum incremental shear strain magnitude near the wall was approximately 2.20%. The presence of these strains was consistent with the rotating principal strains at depths below the excavation base (Finno and Nerby 1989a). The shear strain near the ground surface ranged from 0.33% to 0.36%, smaller compared to that behind the maximum wall deformation. This suggested that the shear plane did not develop to the ground surface; otherwise, the larger shear strain or cracks would be observed at the ground surface.

Distribution of lateral earth pressure

Figure 13 shows the measured strut loads and lateral earth pressure at stage 3(a). Notably, the second strut, positioned proximate to the point of maximum wall deformation, functioned as the primary support, bearing a load of 4868 kN. In contrast, the load on the first strut was comparatively lesser, approximately 1066 kN. It was observed that the lateral earth pressure approximately 9 m below the surface exhibited a decrease, whereas there was an increase in earth pressure in the shallower overlying parts. This phenomenon has been also observed by Ou et al. (1998), Ng and Yan (1998), Ma et al. (2010), and Tan and Wang (2013b). The observed pattern of stress was associated with the arching effect, which could be understood as examining the soil deformations as the excavation proceeded. Once the topmost strut was installed and tightly wedged against the wall, it prevented any further appreciable horizontal displacement of the soil at that depth. As the soil was excavated at a lower depth, the remaining soil at that level moved inward until it was prevented by the middle strut. As a result, the overall pattern of soil movement took on a deep-seated pattern. The larger inward movements of the soil behind the maximum wall deformation led to the resistance of shear stress between the contact parts, further causing stress transfer and exerting drag-type shear stress on the overlying soil. Hence, the soil near the top of the wall was in a more passive stress state rather than an active state of stress.

As depicted in Fig. 14, the lateral earth pressure ratio was defined as the ratio of the lateral earth pressure after excavation to that before excavation. In the shallow soil, the R_a values increased, with a decreasing trend of increment as

Fig. 13. Distribution of lateral earth pressures and horizontal strut loads on Section X2 + 152.

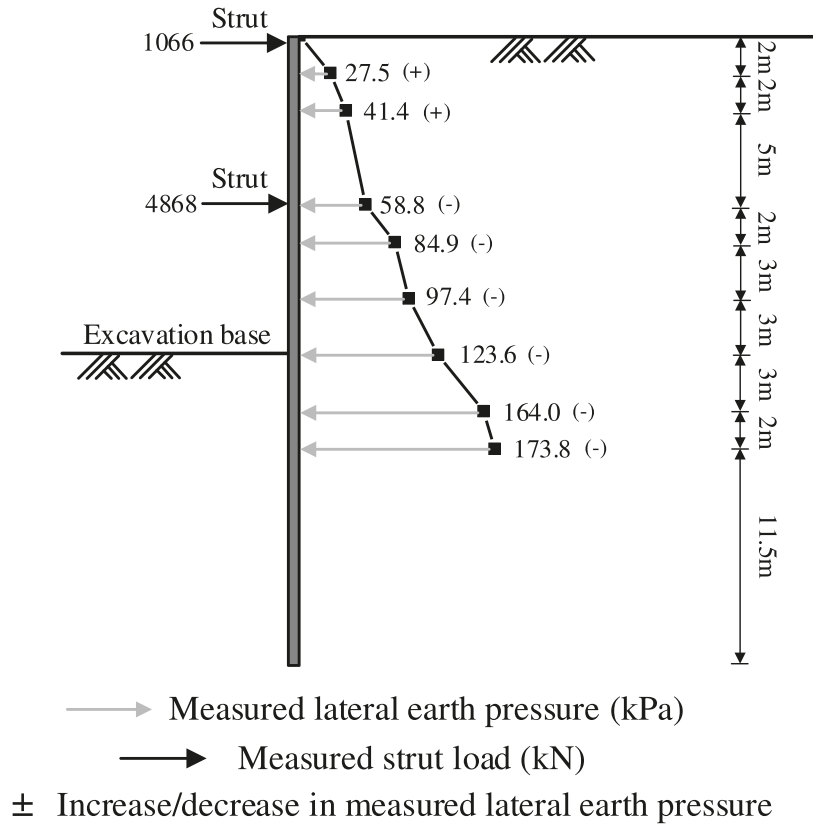
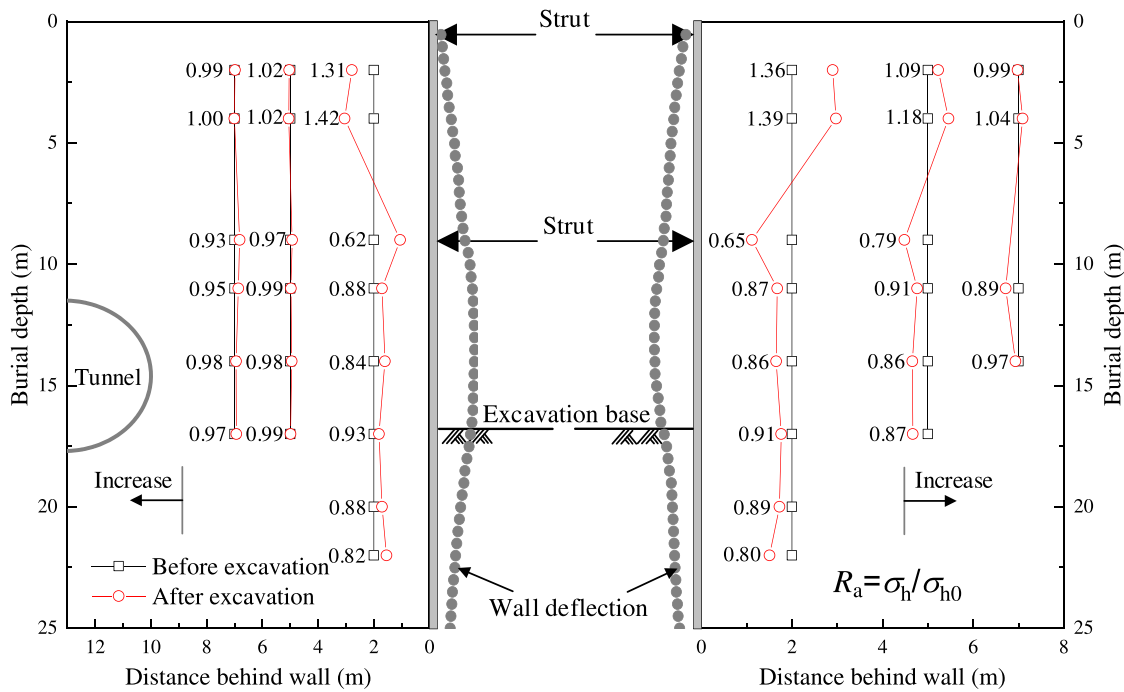


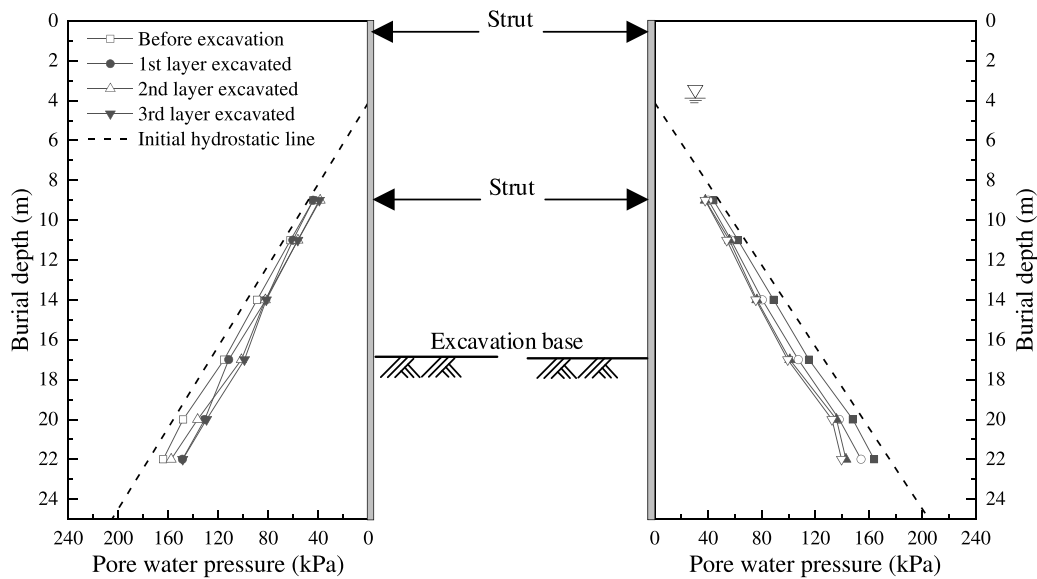
Fig. 14. Distribution of lateral earth pressure ratio (R_a distribution) on Section X2 + 152.



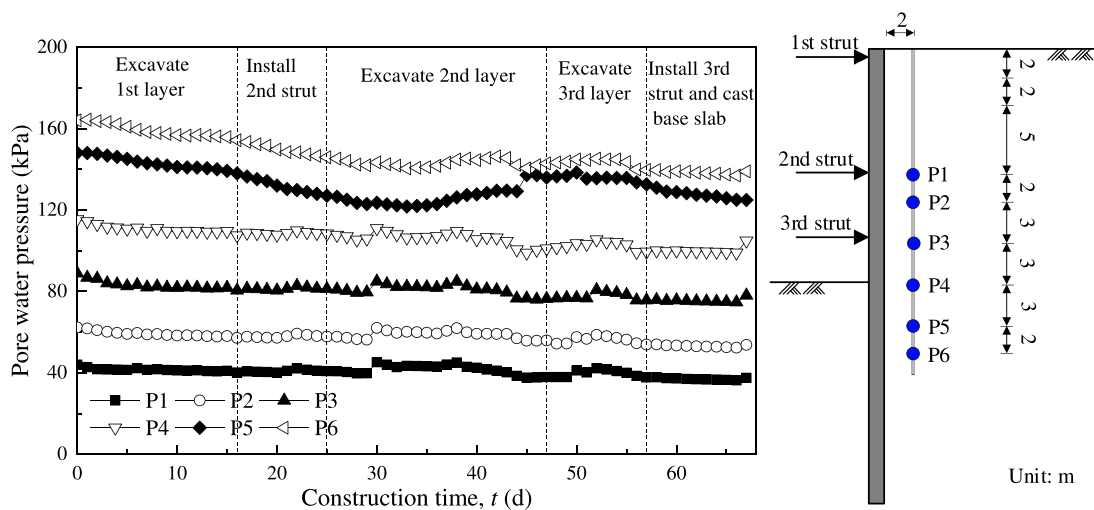
the distance increased. In the deep soil, the degree of lateral earth pressure reduction varied, with the maximum R_a reduction of 0.62 occurring behind the maximum wall deformation. This area experienced the highest shear strain

and the potential sliding plane passed through, which indicated stress redistribution occurring. Both sides of the excavation were asymmetric, with a shield tunnel located approximately 10 m away from the left side. However, the R_a

Fig. 15. (a) Distribution of the pore pressure at different excavation phases on both sides of the excavation and (b) changes of pore pressure on the right side throughout construction.



(a)



(b)

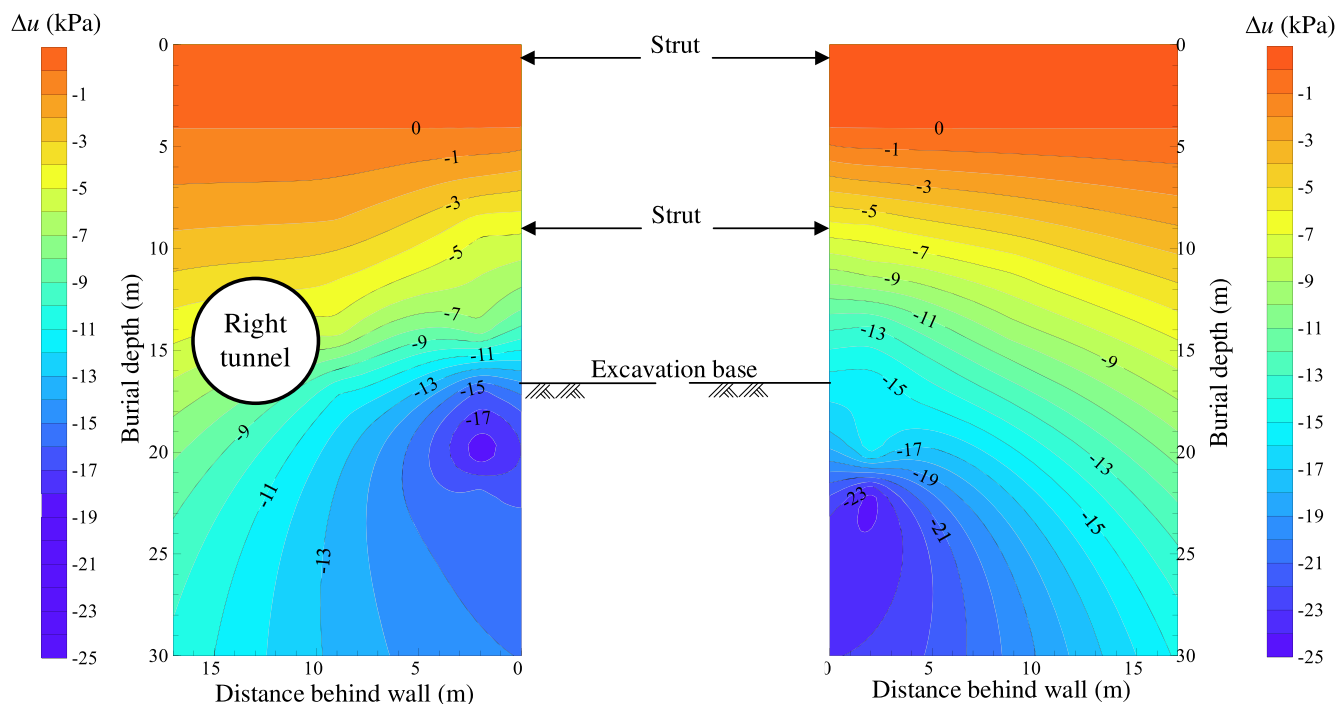
values varied at a distance of 5 m from both sides of the excavation. On the right side of the excavation, the R_a values decreased, with a maximum reduction of 0.79. In contrast, R_a values on the left side remained relatively unchanged, which was an interesting phenomenon. This was related to the interaction between the soil arching induced by the lateral excavation and the shield tunneling-induced soil arching. The shield tunneling induced the soil arching effect, resulting in stress redistribution within the surrounding soil. The subsequent lateral excavation led to another stress redistribution (soil arching effect). The interaction between the two arching effects eventually formed a relatively stable arching in the middle, resulting in little stress change in that area. If the stable arching was not formed, the excavation-induced unloading could cause a reduction in lateral earth pressure.

Pore water pressure

Due to the absence of dewatering processes during the excavation phase, it can be logically inferred that the water table on the retained side remained stable. Consequently, the variations in pore water pressure observed at this site were predominantly the result of excavation-induced load release and subsequent stress redistribution.

As shown in Fig. 15a, the initial pore water pressure fell behind the initial hydrostatic line, indicating that excess pore water pressures induced by diaphragm walling and base reinforcement were fully dissipated before excavation. The measured pore water pressure decreased gradually as the excavation progressed, which could be attributed to the excavation-induced stress release. The pore pressure at 17 and 22 m below the surface decreased by 15.9 and 24.4 kPa, respectively. The pore water pressure decreased more with increas-

Fig. 16. Contour of pore pressure variations on Section X2 + 152.



ing depth due to larger stress release in the deeper soil. As shown in Fig. 15b, two periods of increases in pore pressure were observed, corresponding to the excavation of the second and third layers, respectively. During both periods, the increases were associated with stress transfer from the lower to the upper parts of the soil, indicative of the soil arching effect. These small increases during excavation occurred immediately after each shear zone developed (Finno et al. 1989b). In fact, a noticeable decrease in pore pressure was observed during the formation of the shear plane. After the completion of shear plane development, there was a gradual increase in pore pressure. This phenomenon was also observed in the case histories reported by Finno et al. (1989b), Ng et al. (2012), and Li et al. (2021).

Figure 16 shows the pore pressure variation contours derived from the observed piezometer and Kriging interpolation for stages 3(a). Excavation caused the pore pressures to decrease with increasing depth and with decreasing distance from the wall. The pore pressure concentration zone was observed below the excavation base. The pore pressure zone was bounded by the horizontal distance less than 20 m from the wall and by the depth approximately less than the wall depth (depth = 33.5 m)

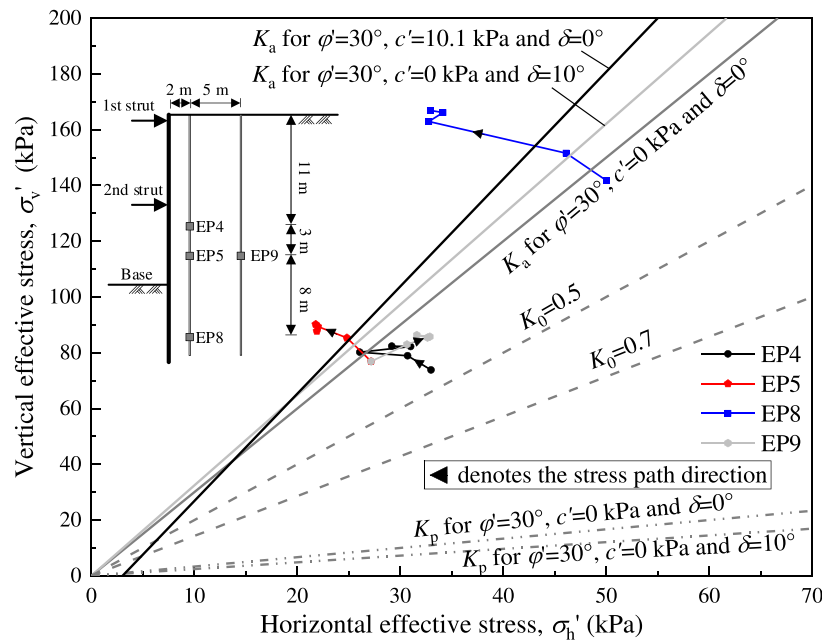
Effective stress path

Figure 17 illustrates some representative effective stress paths at stages 0(c), 1(a), 2(a), 3(a), and 3(c), derived from measurements of total lateral earth pressure σ_h and pore pressures u , assuming that the initial total vertical stress was controlled by the weight of the overlying soil. The horizontal effective stress σ'_h was calculated using the measured total lateral earth pressure and corresponding pore water pressure.

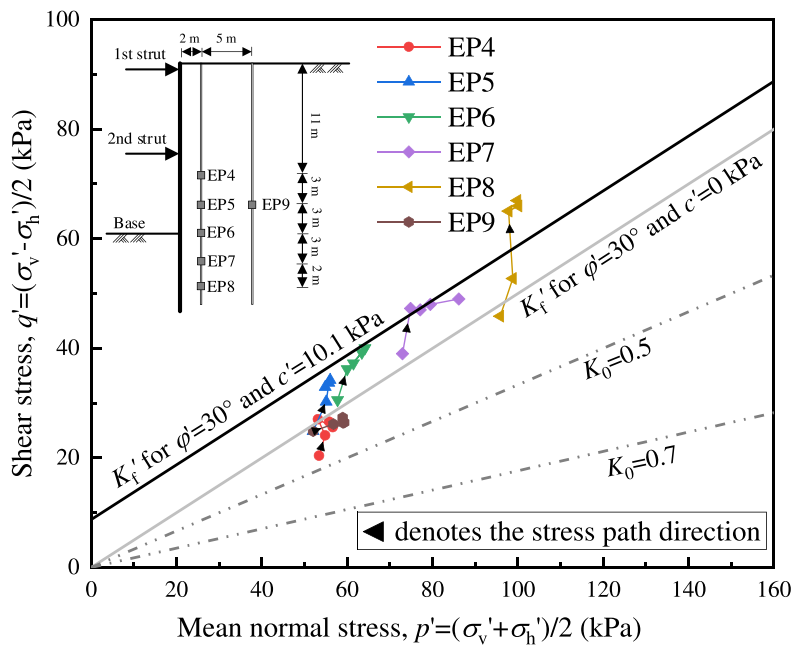
The vertical total lateral stress σ_v was assumed to be constant, and the changes in vertical effective stress σ'_v were only caused by corresponding pore water pressure. The lateral earth pressure coefficient K_0 was considered as 0.7, because of the construction of the diaphragm wall (Ng et al. 2012). Therefore, the initial σ_v could be back-calculated from the corresponding initial σ_h . Besides, the at-rest earth pressure line (K_0 line), failure line (K_f line), and Rankine's passive and active limiting pressures with and without considering soil-wall friction were included in Fig. 17. The average effective inner friction angle, ϕ' (i.e., 30.0°), the average effective cohesion, c' (i.e., 10.1 kPa), and the soil-wall friction angle δ' taken as one-third of ϕ' (i.e., 10°) were taken from Table 1 for calculating the limiting pressures. The arrows in the figure represent the direction of soil stress paths.

As shown in Fig. 17a, the effective stress path at EP5 and EP8 exhibited a decrease in σ'_h (due to lateral stress relief) and an increase in σ'_v (due to the decrease in pore pressure) during excavation. At stage 2(a), the stress path intersected the active limiting line, indicating an active stress state in the soil located both behind the maximum wall deformation (near the wall at EP5) and along the shear plane (at EP8). This result was consistent with Lambe and Whitman (1969), who stated that the state of stress in the soil behind a braced cut has often been described as an arching active condition. Furthermore, the stress path recorded at EP8 closely resembled that observed in the EP6(R) from the soft clay excavation in Ng et al. (2012), indicating similar stress behavior in the excavation. However, the effective stress path at EP9 first showed an increase in σ'_h (due to lateral stress relief less than the pore pressure decrease) and σ'_v (due to the pore pressure de-

Fig. 17. Effective stress paths: (a) relationship between effective horizontal stress and effective vertical stress and (b) relationship between mean normal stress and shear stress. EP, earth pressure cell.



(a)



(b)

crease). The effective stress path at EP9 moved toward the active limiting line but did not reach it, suggesting that the soil behind the maximum wall deformation but far from the wall was not in an active state of stress. The effective stress paths at EP4 near the second strut first showed a decrease in σ'_h and an increase in σ'_v , and experienced a reversal in the direction of the stress path after crossing the K_a line without considering c' and δ' , and then turning to an increase in both

σ'_h and σ'_v . This indicated that soil at EP4 approached the active failure state during excavation.

As shown in Fig. 17b, the effective stress path at EP5, EP6, EP7, and EP8 registered an increase in mean normal stress p' and shear stress q' , and roughly all crossed the K_f line considering c' and ϕ' . This meant that the soils at these points reached the shear strength limit and were in the failure state, which was consistent with the results in Fig. 17a. The effec-

tive stress path at EP4 and EP9 showed an increase in p' and q' , but both did not cross the K_f line with considering c' . Besides, a reversal in the effective stress path at EP4 was observed. This was also consistent with the results in Fig. 17a, where the soils at EP4 and EP9 were approached but not in an active failure state.

Conclusions

This study focuses on the observed transverse ground movement and stress redistribution associated with the arching effect behind the braced excavation, including ground deformation, soil displacement vector, strain path, principal strain, maximum shear strain, lateral earth pressure, pore water pressure, and effective stress path. Based on the field observations and further analyses, the following conclusions can be drawn.

- (1) The diaphragm wall and the ground near the wall exhibited inward deep-seated deformations. The maximum wall deflection recorded was 16.7 mm, which accounts for approximately 0.1% of the excavation depth. The soil displacement behind the maximum wall deformation was greater than that at the neighboring parts, resulting in the resistance of shear strength and the stress transfer from the soil behind maximum deformation to the adjacent relative stationary parts.
- (2) There was a tendency for the soil displacement vectors to be oriented toward the excavation base. The movements above the excavation base were oriented at approximately 45° and indicated progressive movements toward the wall. These incremental movements were indicative of a block-type movement associated with the development of a shearing plane. The horizontal soil displacements near the wall were observed considerably larger than the vertical displacements and the ratio of vertical displacement to horizontal displacement increased with the distance from the wall.
- (3) The majority of the soil behind the wall experienced volumetric expansion. This suggested that the soil volume change has been influenced by consolidation, creep behavior, or a combination of both. Besides, the soil located below the excavation base and passed through by the shear plane had the maximum shear strain of 0.42%. The orientations of the principal strain increments were observed to be significantly more inclined compared to other parts within the soil. This inclination was closely associated with the formation of the shear plane.
- (4) Two periods of increases in pore pressure were associated with stress transfer from the lower to the upper parts (i.e., soil arching effect). In the course of shear plane development, there was a discernible decrease in pore pressure. Conversely, following the formation of the shear plane, a gradual increment in pore pressure was observed. The pore pressure variation zone was characterized by a horizontal extent not exceeding 20 m from the wall, and a vertical limit roughly less than the depth of the wall.
- (5) The soil behind the maximum wall deformation and near the wall and soil below the excavation base and passed

through by the shear plane were in an active stress state. The soil behind the maximum wall deformation but far from the wall did not reach the active state of stress. The lateral earth pressure at 5 m from the left wall of the excavation remained relatively unchanged due to the interaction between the lateral excavation-induced soil arching and the shield tunneling-induced soil arching.

Acknowledgements

The work presented in this paper is financially supported by the National Natural Science Foundation of China (grant Nos. 51938005, 52378338, 52090082, and 52108318) and the Wuhan Municipal Construction Group Company Limited. In addition, the authors are grateful to Mr. Yaoming Tang from Hunan University for his help in the field test.

Article information

History dates

Received: 3 May 2023

Accepted: 5 February 2024

Accepted manuscript online: 9 March 2024

Version of record online: 19 September 2024

Copyright

© 2024 The Author(s). Permission for reuse (free in most cases) can be obtained from [copyright.com](https://www.copyright.com).

Data availability

Data will be made available on request.

Author information

Author ORCIDs

Zhen Liu <https://orcid.org/0009-0005-6222-061X>

Renpeng Chen <https://orcid.org/0000-0001-6968-4955>

Author contributions

Conceptualization: ML, FM

Data curation: ML

Formal analysis: ML, ZL

Funding acquisition: FM, RC

Investigation: FM

Methodology: ML, FM

Project administration: FM, RC

Software: ML

Supervision: FM, ZL

Visualization: ML

Writing – original draft: ML

Writing – review & editing: ML, FM, ZL

Competing interests

The authors declare that they have no known competing financial interests or personal relationships that could have appeared to influence the work reported in this paper.

References

- Becker, D.E., Crooks, J.H.A., Been, K., and Jefferies, M.G. 1987. Work as a criterion for determining in situ and yield stresses in clays. *Canadian Geotechnical Journal*, **26**(2): 327–328. doi:10.1139/t89-042.
- Bolton, M.D. 1993. Mechanisms of ground deformation due to excavation in clay. In *Proc. KIGForum '93: Excavation in Urban Areas*. Japanese Society Soil Mechanics and Foundation Engineering. pp. 1–33
- Bolton, M.D., Lam, S.-Y., Vardanega, P.J., Ng, C.W.W., and Ma, X. 2014. Ground movements due to deep excavations in Shanghai: design charts. *Frontiers of Structural and Civil Engineering*, **8**(3): 201–236. doi:10.1007/s11709-014-0253-y.
- Chen, R.P., Liu, M.C., Meng, F.Y., Wu, H.N., and Li, Z.C. 2023. Soil arching effect associated with ground movement and stress transfer adjacent to braced excavation in clayey ground. *Journal of Geotechnical and Geoenvironmental Engineering*, **149**(12): 04023113. doi:10.1061/JGGEFK.GTENG-11236.
- Cheng, H.Z., Chen, R.P., Wu, H.N., and Meng, F.Y. 2020. A simplified method for estimating the longitudinal and circumferential behaviors of the shield-driven tunnel adjacent to a braced excavation. *Computers and Geotechnics*, **123**: 103595. doi:10.1016/j.compgeo.2020.103595.
- Clough, G.W., and O'Rourke, T.D. 1990. Construction induced movements of in situ walls. In *Proceedings of the ASCE Conference on Design and Performance of Earth Retaining Structures*. ASCE, New York. pp. 439–470.
- Faustin, N.E., Elshafie, M.Z.E.B., and Mair, R.J. 2017. Centrifuge modelling of shaft excavations in clay. In *Proceedings of 9th International Symposium on Geotechnical Aspects of Underground Construction in Soft Ground*, TC204 ISSMGE—IS-Sao Paulo 2017.
- Finno, R.J., and Nerby, S.M. 1989a. Saturated clay response during braced cut construction. *Journal of Geotechnical Engineering*, **115**(8): 1065–1084. doi:10.1061/(ASCE)0733-9410(1989)115:8(1065).
- Finno, R.J., Atmatzidis, D.K., and Perkins, S.B. 1989b. Observed performance of a deep excavation in clay. *Journal of Geotechnical Engineering*, **115**(8): 1045–1064. doi:10.1061/(ASCE)0733-9410(1989)115:8(1045).
- Hashash, Y.M., and Whittle, A.J. 2002. Mechanisms of load transfer and arching for braced excavations in clay. *Journal of Geotechnical and Geoenvironmental Engineering*, **128**(3): 187–197. doi:10.1061/(ASCE)1090-0241(2002)128:3(187).
- Hong, Y., Ng, C.W.W., Liu, G.B., and Liu, T. 2015. Three-dimensional deformation behaviour of a multi-propped excavation at a “greenfield” site at Shanghai soft clay. *Tunnelling and Underground Space Technology*, **45**: 249–259. doi:10.1016/j.tust.2014.09.012.
- Hsieh, P.G., and Ou, C.Y. 1998. Shape of ground surface settlement profiles caused by excavation. *Canadian Geotechnical Journal*, **35**(6): 1004–1017. doi:10.1139/t98-056.
- Karlsrud, K., and Andresen, L. 2005. Loads on braced excavations in soft clay. *International Journal of Geomechanics*, **5**(2): 107–113. doi:10.1061/(ASCE)1532-3641(2005)5:2(107).
- Kung, G.T.C., Juang, C.H., Hsiao, E.C.L., and Hashash, Y.M.A. 2007. Simplified model for wall deflection and ground-surface settlement caused by braced excavation in clays. *Journal of Geotechnical and Geoenvironmental Engineering*, **133**(6): 731–747. doi:10.1061/(ASCE)1090-0241(2007)133:6(731).
- Lambe, T.W., and Whitman, R.V. 1969. *Soil mechanics*. John Wiley and Sons Inc.
- Lei, G.H., Ng, C.W.W., and Rigby, D.B. 2001. Stress and displacement around an elastic artificial rectangular hole. *Journal of Engineering Mechanics*, **127**(9): 880–890. doi:10.1061/(ASCE)0733-9399(2001)127:9(880).
- Li, Z.F., Lin, W.A., Ye, J.N., Chen, Y.M., Bian, X.C., and Gao, F. 2021. Soil movement mechanism associated with arching effect in a multi-strutted excavation in soft clay. *Tunnelling and Underground Space Technology*, **110**: 103816. doi:10.1016/j.tust.2021.103816.
- Liu, G.B., Ng, C.W.W., and Wang, Z.W. 2005. Observed performance of a deep multi-strutted excavation in Shanghai soft clays. *Journal of Geotechnical and Geoenvironmental Engineering*, **131**(8): 1004–1013. doi:10.1061/(ASCE)1090-0241(2005)131:8(1004).
- Liu, G.B., Jiang, R.J., Ng, C.W.W., and Hong, Y. 2011. Deformation characteristics of a 38 m deep excavation in soft clay. *Canadian Geotechnical Journal*, **48**(5): 1817–1828. doi:10.1139/t11-075.
- Liu, M.C. 2022. Soil arching effect and mechanical responses of the existing shield tunnel due to lateral braced excavation. Dissertation for Master Degree. Hunan University, China.
- Liu, M.C., Meng, F.Y., Chen, R.P., Cheng, H.Z., and Li, Z.C. 2023. Numerical study on the lateral soil arching effect and associated tunnel responses behind braced excavation in clayey ground. *Transportation Geotechnics*, **40**: 100970. doi:10.1016/j.trge.2023.100970.
- Ma, W. 2021. Behavior of aged reinforced concrete columns under high sustained concentric and eccentric loads [Doctoral dissertation, University of Nevada, Las Vegas]. Digital Scholarship@UNLV.
- Ma, X.F., Zhang, H.H., Yu, L., Lam, S.Y., and Bolton, M.D. 2010. Case study on a deep excavation in soft ground by centrifuge model tests. In *Proceedings of the 7th International Conference on Physical Modelling in Geotechnics*. Zurich. pp. 487–492
- Meng, F.Y., Chen, R.P., and Kang, X. 2018. Effects of tunneling-induced soil disturbance on post-construction settlement in structured soft soils. *Tunnelling and Underground Space Technology*, **80**: 53–63. doi:10.1016/j.tust.2018.06.007.
- Meng, F.Y., Chen, R.P., Liu, S.L., and Wu, H.N. 2021. Centrifuge modeling of ground and tunnel responses to nearby excavation in soft soil. *Journal of Geotechnical and Geoenvironmental Engineering*, **147**(3): 04020178. doi:10.1061/(ASCE)GT.1943-5606.0002473.
- Meng, F.Y., Chen, R.P., Xie, S.W., Wu, H.N., Liu, Y., and Lin, X.T. 2022b. Excavation-induced arching effect below base level and responses of long-collinear underlying existing tunnel. *Tunnelling and Underground Space Technology*, **123**: 104417. doi:10.1016/j.tust.2022.104417.
- Meng, F.Y., Chen, R.P., Xu, Y., Wu, K., Wu, H.N., and Liu, Y. 2022a. Contributions to responses of existing tunnel subjected to nearby excavation: a review. *Tunnelling and Underground Space Technology*, **119**: 104195. doi:10.1016/j.tust.2021.104195.
- Mindlin, R.D. 1936. Forces at a point in the interior of a semi-infinite solid. *Journal of Applied Physics*, **7**(5): 195–202.
- Ng, C.W.W., and Yan, W.M. 1998. Stress transfer and deformation mechanisms around a diaphragm wall panel. *Journal of Geotechnical and Geoenvironmental Engineering*, **124**(7): 638–648. doi:10.1061/(ASCE)1090-0241(1998)124:7(638).
- Ng, C.W.W., Simons, N., and Menzies, B. 2003. *Soil-structure engineering of deep foundations, excavations, and tunnels*. Thomas Telford.
- Ng, C.W.W., Hong, Y., Liu, G.B., and Liu, T. 2012. Ground deformations and soil-structure interaction of a multi-propped excavation in Shanghai soft clays. *Géotechnique*, **62**(10): 907–921. doi:10.1680/geot.10.P.072.
- Osman, A.S., and Bolton, M.D. 2005. Ground movement predictions for braced excavations in clay. *Journal of Geotechnical and Geoenvironmental Engineering*, **132**(4): 465–477. doi:10.1061/(ASCE)1090-0241(2006)132:4(465).
- Ou, C.Y. 2014. *Deep excavation: theory and practice*. CRC Press.
- Ou, C.Y., Hsien, P.G., and Chiou, D.C. 1993. Characteristic of ground surface settlement during excavation. *Canadian Geotechnical Journal*, **30**(5): 758–767. doi:10.1139/t93-068.
- Ou, C.Y., Liao, J.T., and Lin, H.D. 1998. Performance of diaphragm wall constructed using top-down method. *Journal of Geotechnical and Geoenvironmental Engineering*, **124**(9): 798–808. doi:10.1061/(ASCE)1090-0241(1998)124:9(798).
- Ou, C.Y., Liao, J.T., and Cheng, W.L. 2000. Building response and ground movements induced by a deep excavation. *Géotechnique*, **50**(3): 209–220. doi:10.1680/geot.2000.50.3.209.
- Peck, R.B. 1969. Deep excavation and tunneling in soft ground. In *Proceedings of the 7th International Conference on Soil Mechanics and Foundation Engineering*. Mexico City: International Society for Soil Mechanics and Foundation Engineering. pp. 225–290.
- Phoon, K.K., and Kulhawy, F.H. 1999. Characterization of geotechnical variability. *Canadian Geotechnical Journal*, **36**(4): 612–624. doi:10.1139/t99-038.
- Sagaseta, C. 1987. Analysis of undrained soil deformation due to ground loss. *Géotechnique*, **37**(3): 301–320. doi:10.1680/geot.1987.37.3.301.
- Schwamb, T., Elshafie, M.Z.E.B., Soga, K., and Mair, R.J. 2016. Considerations for monitoring of deep circular excavations. *Proceedings of the Institution of Civil Engineers: Geotechnical Engineering*, **169**(6): 477–493.

- Tan, Y., and Li, M. 2011. Measured performance of a 26 m deep top-down excavation in downtown Shanghai. *Canadian Geotechnical Journal*, **48**(3): 704–719. doi:[10.1139/t10-100](https://doi.org/10.1139/t10-100).
- Tan, Y., and Wang, D.L. 2013a. Characteristics of a large-scale deep foundation pit excavated by the central-island technique in Shanghai soft clay. I: bottom-up construction of the central cylindrical shaft. *Journal of Geotechnical and Geoenvironmental Engineering*, **139**(11): 1875–1893. doi:[10.1061/\(ASCE\)GT.1943-5606.0000928](https://doi.org/10.1061/(ASCE)GT.1943-5606.0000928).
- Tan, Y., and Wang, D.L. 2013b. Characteristics of a large-scale deep foundation pit excavated by the central-island technique in Shanghai soft clay. II: top-down construction of the peripheral rectangular pit. *Journal of Geotechnical and Geoenvironmental Engineering*, **139**(11): 1894–1910. doi:[10.1061/\(ASCE\)GT.1943-5606.0000929](https://doi.org/10.1061/(ASCE)GT.1943-5606.0000929).
- Tan, Y., and Wei, B. 2012. Observed behaviors of a long and deep excavation constructed by cut-and-cover technique in Shanghai soft clay. *Journal of Geotechnical and Geoenvironmental Engineering*, **138**(1): 69–88. doi:[10.1061/\(ASCE\)GT.1943-5606.0000553](https://doi.org/10.1061/(ASCE)GT.1943-5606.0000553). PMID: [34916772](https://pubmed.ncbi.nlm.nih.gov/34916772/).
- Terzaghi, K. 1943. *Theoretical soil mechanics*. John Wiley and Sons.
- Trochu, F. 1993. A contouring program based on dual kriging interpolation. *Engineering with Computers*, **9**(3): 160–177. doi:[10.1007/BF01206346](https://doi.org/10.1007/BF01206346).
- Yang, H., Tan, T.S., and Leung, C.F. 2011. Mass behaviour of embedded improved soil raft in an excavation. *Proceedings of the Institution of Civil Engineers—Geotechnical Engineering*, **164**(1): 11–25. doi:[10.1680/geng.9.00078](https://doi.org/10.1680/geng.9.00078).
- Yang, K., Li, Z., Chen, Y., Yang, X., and Lin, W. 2023. Soil arching-Induced lateral earth pressure redistribution on the retaining wall in a multistrutted excavation in soft Soil. *Journal of Geotechnical and Geoenvironmental Engineering*, **149**(10): 05023004. doi:[10.1061/JGGEFK.GTENG-11032](https://doi.org/10.1061/JGGEFK.GTENG-11032).
- Zhu, M., Gong, X.N., Gao, X., Liu, S.M., and Yan, J.J. 2019. Remediation of damaged shield tunnel using grouting technique: serviceability improvements and prevention of potential risks. *Journal of Performance of Constructed Facilities*, **33**(6): 04019062. doi:[10.1061/\(ASCE\)CF.1943-5509.0001335](https://doi.org/10.1061/(ASCE)CF.1943-5509.0001335).